Dalton Transactions

The Effect of Mg_3As_2 Alloying on the Thermoeelctric Properties of n-type $Mg_3(Sb, Bi)_2$

Journal:	*Dalton Transactions*
Manuscript ID	DT-COM-05-2021-001600.R1
Article Type:	Communication
Date Submitted by the Author:	14-Jun-2021
Complete List of Authors:	Imasato, Kazuki; Northwestern University , Materials Science and Engineering; National Institute of Advanced Industrial Science and Technology Tsukuba Center Tsukuba Central, Global Zero Emission Research Center Anand, Shashwat; Northwestern University, Materials Science and Engineering Gurunathan, Ramya; Northwestern University, Materials Science and Engineering Snyder, G.; Northwestern University, Materials Science

Journal Name

ARTICLE TYPE

Cite this: DOI: 00.0000/xxxxxxxxxx

The Effect of Mg_3As_2 Alloying on the Thermoelectric Properties of n-type $Mg_3(Sb, Bi)_2$

Kazuki Imasato,[a,b*] Shashwat Anand,[a], Ramya Gurunathan,[a] and G. Jeffrey Snyder[a*]

Received Date
Accepted Date

DOI: 00.0000/xxxxxxxxxx

$Mg_3Sb_2-Mg_3Bi_2$ alloys have been heavily studied as a competitive alternative to the state-of-the-art n-type $Bi_2(Te,Se)_3$ thermoelectric alloys. Using Mg_3As_2 alloying, we examine another dimension of exploration in $Mg_3Sb_2-Mg_3Bi_2$ alloys and the possibility of further improvement of thermoelectric performance was investigated. While the crystal structure of pure Mg_3As_2 is different from Mg_3Sb_2 and Mg_3Bi_2, at least 15% arsenic solubility on the anion site ($(Mg_3((Sb_{0.5}Bi_{0.5})_{1-x}As_x)_2$: x=0.15) was confirmed. Density functional theory calculations showed the possibility of band convergence by alloying $Mg_3Sb_2-Mg_3Bi_2$ with Mg_3As_2. Because of only a small detrimental effect on the charge carrier mobility compared to cation site substitution, the As 5% alloyed sample showed zT=0.6-1.0 from 350 K to 600 K. This study shows that there is an even larger composition space to examine for the optimization of material properties by considering arsenic introduction into the $Mg_3Sb_2-Mg_3Bi_2$ system.

n-type $Mg_3Sb_2-Mg_3Bi_2$ alloys have attracted significant attention as they are one of the most potent thermoelectric materials in the low (near room temperature) to mid-temperature (≈700 K) range[1–4] because of their highly degenerate conduction band structure[1,2,5] and extremely low phonon thermal conductivity.[6] Since the discovery of n-type $Mg_3Sb_{1.5}Bi_{0.5}$ with zT of 1.6 at 700 K in 2016,[1] extensive research has been conducted to optimize their thermoelectric performance by engineering the electronic band structure,[7,8] chemical doping,[9–15] and optimization of microstructure.[16–20] Further improvements in the performance could lead to new opportunities for energy harvesting and IoT (Internet of things) devices being made using this system which has better mechanical properties[21,22] and consists of abundant elements compared to commercially used Bi_2Te_3-based materials.[23–25]

The crystal structure of Mg_3Sb_2 (space group $P\bar{3}m1$ No. 164) which has two Mg sites, octahedrally coordinated Mg(1), and tetrahedrally coordinated Mg(2) is shown in Figure 1(a). Mg_3Bi_2 has the same crystal structure as Mg_3Sb_2, and makes a complete solid solution within the entire composition range. In addition to a more than 50 % reduction in the lattice thermal conductivity with alloy scattering, Mg_3Bi_2 alloying (Bi alloying) was proven to be an effective way to improve thermoelectric performance by optimizing the electronic band structure.[7,8,26] Alloying Mg_3Sb_2 with Mg_3Bi_2 produces a higher mobility, a shift of the peak zT with temperature and a reduced band gap.[8,23,26] On the other hand, the substitution of the cation (Mg) site with other elements causes a significant reduction in the thermoelectric performance due to a decreased charge carrier mobility.[11,27] This degraded performance is mainly attributed to the disruption in the conduction band which originates from Mg orbital interaction.[11,28] This result suggests that alloying on the anion site should be a better method to improve performance without hurting the electronic mobility, which is recognized as the reason for significant success with Bi content optimization.[8,29–31] Based on this argument, arsenic alloying on the anion site is chosen, as arsenic is in the same group as Sb and Bi, as a straightforward way to enhance thermoelectric performance. However, there are no

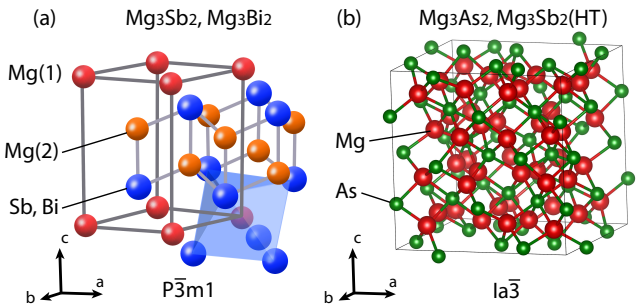

Fig. 1 (a) Crystal structure of $Mg_3(SbBi)_2$ (space group $P\bar{3}m1$ [164]) and (b) Mg_3As_2 (space group $Ia\bar{3}$ [206]). The high temperature phase of Mg_3Sb_2, stable above 1193 K also has the $Ia\bar{3}$ structure. There are two Mg sites in the $P\bar{3}m1$ structure, the octahedrally coordinated Mg(1), and the tetrahedrally coordinated Mg(2), whereas the $Ia\bar{3}$ structure has only tetrahedral Mg sites.

[a] *Department of Materials Science and Engineering, Northwestern University, Evanston, Illinois 60208, USA. E-mail: jeff.snyder@northwestern.edu*
[b] *Global Zero Emission Research Center, National Institute of Advanced Industrial Science and Technology (AIST), Tsukuba, Ibaraki 305-8569, Japan*

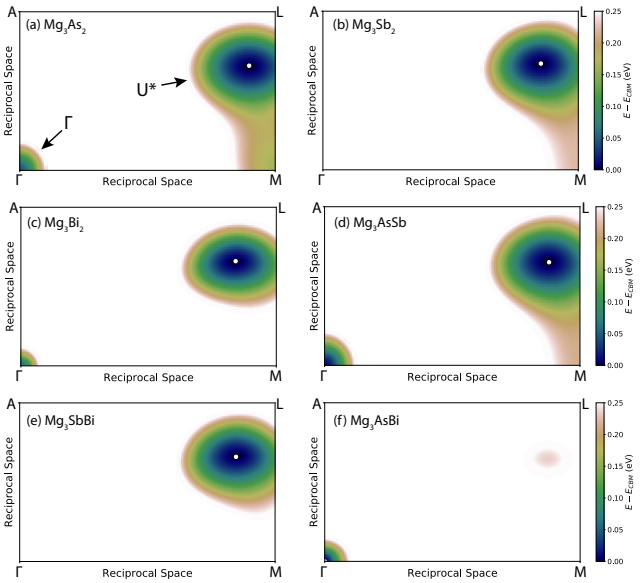

Fig. 2 The conduction band electron energy contour plot for (a)Mg_3As_2, (b)Mg_3Sb_2, (c)Mg_3Bi_2, (d)Mg_3AsSb, (e)Mg_3SbBi and (f)Mg_3AsBi in the Γ–A–L–M plane of reciprocal space. The color scale varies over the range [0 to 0.25eV into the conduction band]. The conduction band minimas are shown by a white circle symbol. The 6-fold degeneracy of the conduction band at U* is beneficial for thermoelectrics while the separate band at Γ has degeneracy of one. Mg_3AsBi shows conduction band minimum (CBM) at Γ which suggests the potential of a band convergence of Γ and U* by changing the ratio of As, Sb, Bi in $Mg_3(As, Sb, Bi)_2$

arsenic alloys reported to date in Mg_3Sb_2-based systems, except for some band structure calculations.[5,22,32]

One of the reasons why As-alloyed Mg_3Sb_2 has not previously been synthesized is that the crystal structure of Mg_3As_2 is different from Mg_3Sb_2 and Mg_3Bi_2.[33–35] The crystal structure of Mg_3As_2 belongs to space group $Ia\bar{3}$ from room temperature up to around 1100 °C, which is different from the $P\bar{3}m1$ space group of the Mg_3Sb_2 and Mg_3Bi_2 structure[33] (Figure 1(b)). This suggests that Mg_3As_2 alloying may be different from the Mg_3Sb_2/Mg_3Bi_2 solid solution case, where you can adjust the Sb/Bi ratio without changing the crystal structure or producing impurity phases. However, the high temperature phase of Mg_3As_2 around 1373 K to 1473 K is actually $P\bar{3}m1$ suggesting that this structure is close to being stable. In addition, the high temperature phase of Mg_3Sb_2 (around 1173 K to 1473 K) is the $Ia\bar{3}$ structure type, the same as the low temperature phase of Mg_3As_2.[34] Considering the pressing temperature around 873K-1073K, we can assume these two crystal structures have very similar formation energies. This suggests that there should be some solubility of arsenic in $Mg_3(Sb, Bi)_2$.

The main motivation for arsenic alloying is potential improvement from band engineering by optimizing the As/Sb/Bi ratio. To see the effect of arsenic alloying on the electronic band structure, density functional theory (DFT) calculations were performed for 6 chosen compositions in the $Mg_3(As,Sb,Bi)_2$ alloy. From the point of view of *n*-type transport, the two main bands to consider are U* and Γ point. Since the position of the conduction band minima located at a non high-symmetry point U* can shift with alloying percentage, we plot the 2 dimensional electron energy band contour plot in the Γ-A-L-M plane (see Figure 2) which contains U*. As reported in the previous studies,[1,36] the conduction minima of Mg_3Sb_2-Mg_3Bi_2 alloys (Figure 2 (b), (c), (e)) are found at a point labeled U* which has band degeneracy of 6. Also, the conduction band minimum in Mg_3As_2 (Figure 2 (a) hexagonal $P\bar{3}m1$ phase) and Mg_3AsSb Figure 2 (b) are at the U* point similar to the Sb-Bi cases, however, only Mg_3AsBi (As:Bi=50:50) displays a minimum at the Γ point shown in Figure 2 (f). This implies a potential band convergence of Γ and U* bands in the pseudo-ternary composition space in $Mg_3(As, Sb, Bi)_2$. We note that the convergence with the Γ band might not be necessarily beneficial because of the effects of intervalley scattering. Nevertheless, since arsenic alloying can also lead to the reduction of the thermal conductivity with more disorder, arsenic alloying opens up an entirely new phase space to optimize thermoelectric performance of $Mg_3(Sb, Bi)_2$ compounds.

Based on these strategies and computational suggestions, we synthesized various compositions of $Mg_3(Sb_{0.5}Bi_{0.5})_2$ alloyed with Mg_3As_2. The Bi:Sb ratio of 50 % composition ($Mg_3(Sb_{0.5}Bi_{0.5})_2$) was chosen as the matrix composition because of its low thermal conductivity and high weighted mobility.[8,31] 5 %, 10%, and 15 % of Mg_3As_2 ($Mg_3((Sb_{0.5}Bi_{0.5})_{1-x}As_x)_2$: x=0.05, 0.1, and 0.15) were added to explore the effect of Mg_3As_2 alloying on the thermoelectric properties of n-type $Mg_3(Sb_{0.5}Bi_{0.5})_2$. As the solubility of arsenic in this system was unknown, we performed X-ray diffraction measurements and microscopic analyses before measuring thermoelectric transport properties. All the XRD peaks can be indexed with the hexagonal $P\bar{3}m1$ crystal structure for x = 0.05-0.15, and there were no impurity peaks within the detection limit of XRD measurements (Figure 3). Lattice constants were calculated by Rietveld refinement to check the effect of arsenic substitution on the unit cell. The linear decrease in lattice constants following Vegard's law suggests the solubility of arsenic is at least up to 15% on the anion site in the crystal structure. The diffraction peak shifts to higher angles as shown in the inset of figure 3(a) indicating a decrease in the unit cell expected from the smaller As atom. To confirm homogeneity, energy-dispersive X-ray spectroscopy (EDS) was performed for the sample with the highest arsenic content (As = 15%). The actual composition measured by EDS is consistent with the nominal composition as listed in table 1. The homogeneous distribution of As, Sb, and Bi observed in the 15 % alloyed sample confirms the successful synthesis of $Mg_3(As,Sb,Bi)_2$.

We investigated the transport properties with different amount of arsenic content x in $Mg_{3.05}((Sb,Bi)_{1-x}As_x)_{1.99}Te_{0.01}$ x=0.05-0.15.(Figure 4) A small amount of Te, which is known to work as an electron donor in this system, is added to tune the carrier concentration.[3,37] The increased absolute value of the Seebeck co-

Table 1 Chemical analysis of $Mg_{3.05}((Sb_{0.5}Bi_{0.5})_{1-x}As_x)_{1.99}Te_{0.01}$: x=0.15, obtained from Energy-dispersive X-ray spectroscopy. Values are consistent with the atomic percentage of the anion site calculated from the nominal composition.

Element	atomic %	atomic % at anion site	nominal composition
Mg	60.1	N/A	N/A
As	6.2	15.6	15.0
Sb	16.8	42.1	42.5
Bi	16.9	42.2	42.5

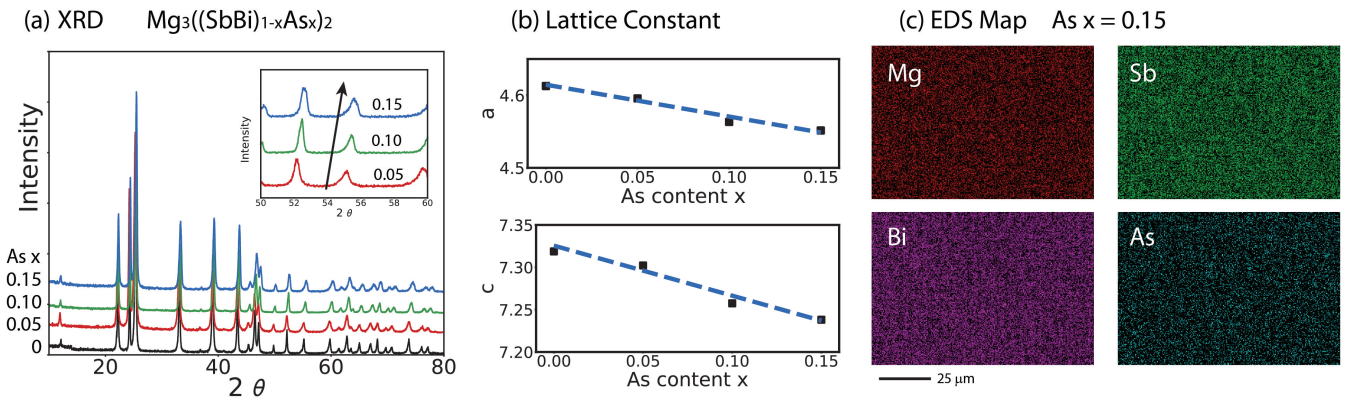

Fig. 3 (a)X-ray diffraction pattern of $Mg_3((Sb,Bi)_{1-x}As_x)_2$: x=0.05-0.15. No impurity peaks were observed. The inset is the enlarged figure for 2θ = 50-60 ° showing the shift of diffraction peaks to higher angle with increasing As content. Data for the sample without As were extracted from ref.[8] (b) Lattice parameters a and c decrease linearly, indicating the inclusion of arsenic in the crystal structure and decent solubility of arsenic. The dashed line is to guide the eye. The goodness of fit factors of Rietveld refinement for teach alloy are 1.95, 1.65, and 2.2 for x = 0.05, 0.1, and 0.15 respectively. (c) Energy-dispersive X-ray spectroscopy (EDS) mapping for the sample with the highest As content x= 0.15, showing the homogeneous distribution of Mg, Sb, Bi, and As.

efficient and decreased electrical conductivity with arsenic content x can be explained by the change in the charge carrier concentration n_H (Figure 4(a)-(c). Interestingly, even though all samples have the same dopant content (Te amount of 0.01), the carrier concentration decreases as arsenic content increases. In the $Mg_3(Sb,Bi)_2$ system, generally, the carrier concentration can be easily controlled by changing the amount of extrinsic dopants.[3,37] The reduction in the carrier concentration can be attributed to either a reduced solubility of Te or a change in the defect formation energy which was also seen in Yb alloyed $Mg_3(Sb,Bi)_2$.[27] Due to the lower carrier concentration with the arsenic content x, the electrical conductivity also decreases. To compare the inherent properties of the material independent from Fermi level or carrier concentration, the weighted mobility was also evaluated.[38–40] The reduction of the weighted mobility was observed as the As content x, increases. However, the extent of the weighted mobility reduction is smaller compared to the substitution with other elements.(Figure 4(d)) Particularly with arsenic content $x = 0.05$, the weighted mobility was reduced by only ≈ 7% at 473 K while, for example, a similar amount of Yb alloying (Yb content 0.075) and La doping (La content 0.01) on the Mg site causes ≈34%, and ≈46% reduction in the weighted mobility, respectively.[11,27] The small effect on the mobility with arsenic alloying is consistent with the idea that the anion substitution affects the conduction band states less than cation site substitution.[11,28]

Although a band convergence effect can be expected from DFT at some $Mg_3(As,Sb,Bi)_2$ alloy compositions, for the compositions synthesized here no significant improvement in the weighted mobility from the band convergence was observed. Neither a peak nor a clear trend in effective mass was confirmed with As content x =0.05, 0.1, and 0.15. Due to the complexity of the system with 4 elements plus a dopant, it is quite possible that the compositions synthesized are somewhat off from the optimum composition. There is a vast composition space in the Mg_3As_2-Mg_3Sb_2-Mg_3Bi_2 system, and the band convergence effect might only be activated in a small window of the composition. Thus, thorough computational and experimental optimizations might be required to fully take advantage of the band structure change in these alloys. Additionally, even though there is no evidence of impurity phases, the formation of impurity could affect the solubility of the extrinsic dopant Te and therefore limit the charge carrier concentration. The problem of the carrier concentration reduction could be avoided by using cation site dopants, which has been suggested as a more effective way to dope Mg_3Sb_2-Mg_3Bi_2 alloys than with Te.[10,11,13]

Despite the larger atomic size difference by having arsenic alloying with antimony or bismuth, a substantial reduction in lattice thermal conductivity with arsenic alloying was not observed. (Figure 4(e) and 5) The lattice thermal conductivity κ_L is estimated by calculating κ_e using the Wiedemann–Franz law, $\kappa_e = L\sigma T$, and subtracting it from the total thermal conductivity κ_{tot}: $\kappa_L = \kappa_{tot}$ - κ_e where L is the Lorentz number. The Lorentz number can be approximated using the experimental Seebeck coefficient.[41,42] The reason for little or no reduction in the lattice thermal conductivity could be due to two reasons: 1. Because the arsenic atom is lighter than the other two anion atoms, Mg_3As_2 is expected to have a higher intrinsic lattice thermal conductivity. Thus, introducing small amounts of arsenic may not reduce the thermal conductivity despite the mass difference among the structure. 2. The matrix composition (Mg_3SbBi) was not the best choice to examine the effect of the lattice thermal conductivity reduction. Since Bi 50% matrix composition (Mg_3SbBi) shows already very small thermal conductivity, the phonon scattering is almost maximized in this atomic configuration. To examine these possibilities, we performed lattice thermal conductivity modeling in the pseudo-ternary phase diagram of $Mg_3(As, Sb, Bi)_2$.

To understand the reason of no reduction in the lattice thermal conductivity κ_L, we computed κ_L values by using the Klemens alloy scattering model in the pseudo-ternary phase diagram of $Mg_3(As, Sb, Bi)_2$.(Figure 5) The Klemens model accounts for phonon scattering due to atomic mass and size variance in the alloy, and we follow the procedure outlined in Ref.[43]. To perform this calculation, we were required to estimate the lattice thermal conductivity of Mg_3As_2 in the $P\bar{3}m1$ structure type, although this is not the sta-

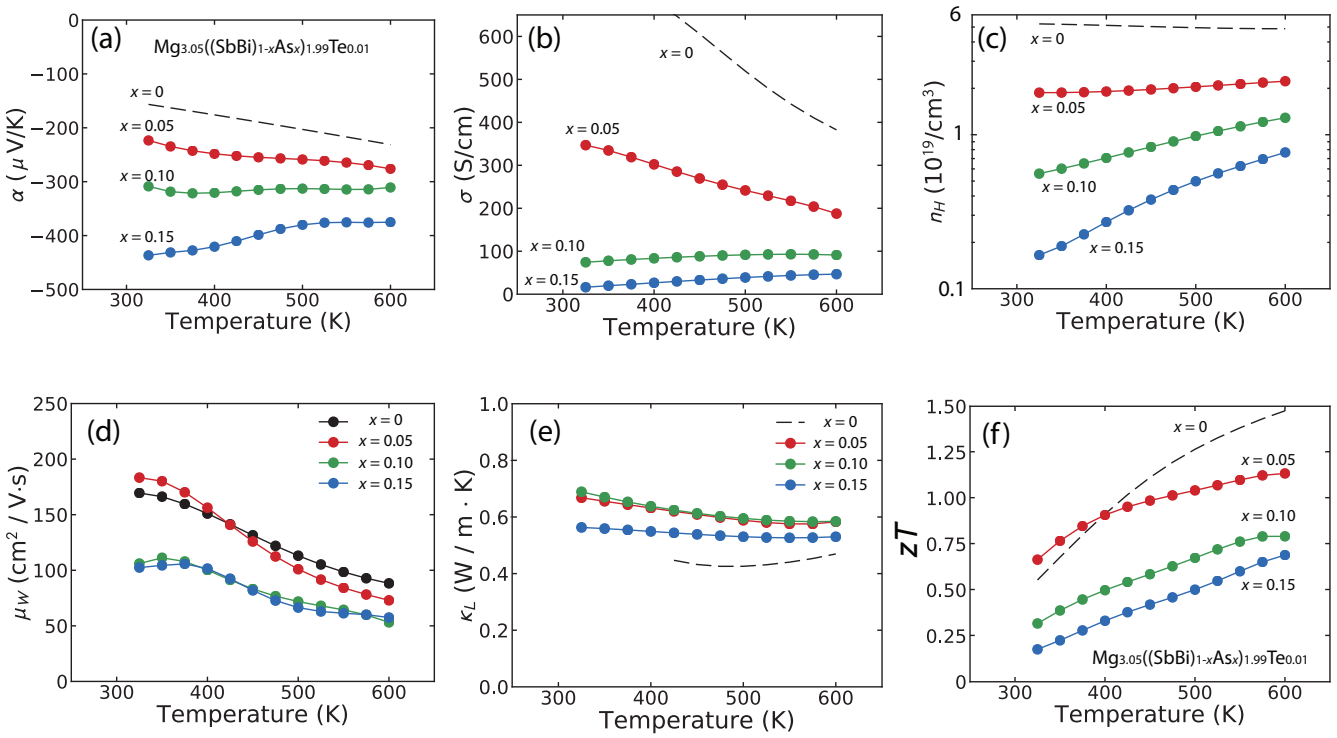

Fig. 4 Thermoelectric transport properties of $Mg_{3.05}(Sb,Bi)_{1-x}As_x)_{1.99}Te_{0.01}$ x=0-0.15 (a) Seebeck coefficient, (b) Hall charge carrier concentration, and (c) electrical conductivity, (d) weighted mobility, (e) lattice thermal conductivity, and (f) figure of merit zT from 300 K to 600K. Data for the sample without As were extracted from our previous study for comparison.[8]

ble phase. The anomalously low thermal conductivity of Mg_3Sb_2 and Mg_3Bi_2 has been attributed to the large anharmonicity of the transverse acoustic modes, which can be rationalized by the structural instabilities of the Mg atom in the octahedral site[44]. The small cation-to-anion ratio violates Pauling's radius ratio stability rules, resulting in a distorted octahedral environment[44]. However, the larger cation-to-anion ratio in Mg_3As_2 is expected to better stabilize the Mg in the octahedral site, leading to lower anharmonicity and higher intrinsic κ_L. The intrinsic Mg_3As_2 κ_L was calculated from the following expression[45,46]:

$$\kappa_L = A\frac{\bar{M}v_s^3}{TV^{2/3}\gamma^2}\left(\frac{1}{N^{1/3}}\right), \quad (1)$$

where $\bar{M}$ is the average atomic mass, v_s is the isotropic speed of sound, V is the volume per atom, γ is the Grüneisen parameter, N is the number atoms per primitive unit cell, and A is a fitting parameter. The speed of sound was calculated from DFT elastic constants, and an estimate Grüneisen parameter of 1.3 was used, which empirical relations show to be a reasonable estimate for mixed tetrahedral and octahedral bonding environments[47]. Finally, the coefficient A was fit to the Mg_3Sb_2 and Mg_3Bi_2 end-member κ_L data. We predict a Mg_3As_2 κ_L value of 4.7 W/m/K, which is significantly larger than that of the other end-members. As depicted in the model predictions (Figure 5), the larger κ_L value for Mg_3As_2 can justify why a reduced thermal conductivity was not observed with the introduction of As to the Mg_3SbBi composition. The model predictions does suggest, however, that alloy compositions richer in Sb could exhibit some reductions in κ_L with the introduction of As.

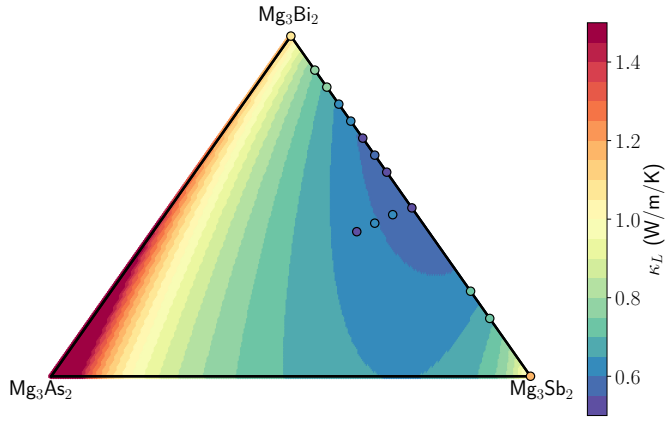

Fig. 5 Lattice thermal conductivity κ_L predictions (heatmap) with overlaid experimental datapoints in the $Mg_3(As, Sb, Bi)_2$ pseudo-ternary space using an analytic alloy model including mass and bond length variance scattering effects. Although Mg_3As_2 is unstable in the $P\bar{3}m1$ phase, we attempt to estimate the thermal conductivity of this structural analog from its DFT elastic constants. We estimate Mg_3As_2 to have a larger κ_L of 4.9 W/m/K such that introducing arsenic slightly increases the κ_L despite the introduction of mass and bond length variance.

Because there are no significant signs of band convergence and reduction in the lattice thermal conductivity, an improvement of

zT was not significant with arsenic alloying on $Mg_3(Sb, Bi)_2$ in this study. (Figure 4(f)) Slightly higher zT values around 350K with arsenic content x = 0.05 compared to no arsenic can be attributed to the difference in the grain boundary effect as it can be seen in the deviation from the temperature dependency of weighted mobility from $T^{-3/2}$ at lower temperature.[16,48](Figure 4(d)) Also, the lower carrier concentration with arsenic content x shifted the peak zT to the lower temperature. Nevertheless, zT = 0.6-1.0 from 350 K to 600 K are decent zT values especially considering the lack of good n-type thermoelectric materials around room temperature to the mid-temperature range.

In conclusion, the possibility of further improving thermoelectric performance of $Mg_3(Sb, Bi)_2$ with arsenic alloying on the anion site has been investigated. While the crystal structure of Mg_3As_2 is different from $Mg_3(Sb, Bi)_2$, at least 15% arsenic solubility on anion site is confirmed. Since the DFT results showed the conduction band minimum of Mg_3AsBi at the Γ point, there is a possibility of band convergence with arsenic alloying with $Mg_3(Sb,Bi)_2$. However, evidence of band convergence was not confirmed with arsenic content x = 0.05-0.15 in $Mg_{3.05}((Sb,Bi)_{1-x}As_x)_{1.99}Te_{0.01}$ and the significant improvement of thermoelectric performance was not confirmed with synthesized samples in this study. Possible reasons for this result is the deviation from the optimum As/Sb/Bi ratio due to the complexity of the system. Nevertheless, the mobility reduction is minimized compared to cation site doping or alloying and relatively high zT = 0.6-1.0 from 350 K to 600 K was achieved. More importantly, proving the solubility of As in Mg_3Sb_2-Mg_3Bi_2 alloys with minimum effect on mobility can lead to an expanded study of Mg_3Sb_2-Mg_3Bi_2 alloys with further trials. To date, research efforts have been heavily focused on trying to investigate the best Sb/Bi ratio in the composition line between Mg_3Sb_2 and Mg_3Bi_2; however, this work proposed a new dimension to explore in the pseudo-ternary composition space in $Mg_3(As,Sb,Bi)_2$.

Methods

Pure elemental materials of magnesium turnings (99.98 %, Alfa Aesar), antimony shots (99.9999 %, Alfa Aesar), bismuth granules (99.997 %, Alfa Aesar) arsenic powder (99 %, Alfa Aesar) and tellurium lumps (99.999 %, Alfa Aesar) were loaded according to the nominal composition and sealed into stainless-steel vials with two half inch stainless-steel balls inside the argon-filled glove box. Mechanical reaction was conducted by high energy-ball milling with a SPEX 8000D mill for two hours. The reacted powder was extracted from vials and transferred into a graphite die under argon atmosphere to prevent the oxidization of the materials. Subsequently, induction heated rapid hot pressing[49] was conducted for 20 min at 1073 K and 45 MPa under argon gas flow to prepare pellet-shaped samples.[50] Pressed samples were gradually cooled down to room temperature with no load. The Seebeck coefficient of each sample was measured with Chromel-Nb thermocouples in a two-probe configuration under high vacuum.[50] The Hall coefficient and electric resistivity was measured simultaneously using a 4-point probe Van der Pauw technique with a 2 T magnetic field under high vacuum.[51] Thermal diffusivity D was measured by using the flash method with a Netzsch LFA 457 under dynamic argon atmosphere. The thermal conductivity κ was calculated by $\kappa = D \times C_p \times d$, where d is the geometrical density (geometric densities are 99 %, 98 %, and 95 % of theoretical density of each alloy for x = 0.05, 0.1, and 0.15 respectively) and C_p is the heat capacity. Physics based empirical model was used to estimate the heat capacity to calculate the thermal conductivity.[52] Energy-dispersive X-ray spectroscopy maps were obtained using a scanning electron microscope (Quanta 650 FEG) equipped with a detector (Oxford Instruments Nordlys) X-ray diffraction of the sample was measured at room temperature on a STOE-STADI MP powder diffractometer. The line focused X-ray tube was operated at 50 kV and 40 mA. The sample was placed on a metallic holder and measured in reflection geometry in a rotating stage.

The density functional theory (DFT) calculation[53] in this study were performed using Vienna ab initio simulation package (VASP).[54] For structural relaxation, we have used Perdew–Burke–Ernzerhof (PBE) formulation of the exchange correlation energy functional derived under a gradient-generalized approximation (GGA).[55] Plane-wave basis sets truncated at a constant energy cutoff of 340 eV were used, as were Γ-centered k-point meshes with a density of ~8000 k-points per reciprocal atom (KPPRA). All structures were relaxed with respect to cell vectors and their internal degrees of freedom until forces on all atoms were less than 0.1 eV nm^{-1}. The electron energy band contour plots were calculated using the mBJ potential[56] including spin-orbit coupling interactions. A simple comparison of the band contour plots requires that the symmetry of the structure and number of atoms at the various compositions stay the same. For this reason, the Mg_3SbBi, Mg_3AsBi, Mg_3SbAs structures are obtained by simply replacing one of the two anion atoms in the end member with the corresponding alloying element. The isotropic speeds of sound of end-members were calculated using the christoffel code.[57] The elastic modulus tensor input for the code was calculated from the Density Functional Perturbation Theory (DFPT) capabilities implemented in VASP.

Conflicts of interest

There are no conflicts to declare

Acknowledgement

GJS, KI acknowledge the support of award 70NANB19H005 from U.S. Department of Commerce, National Institute of Standards and Technology as part of the Center for Hierarchical Materials Design (CHiMaD) The IMSERC X-ray Facility at Northwestern University is supported by the Soft and Hybrid Nanotechnology Experimental (SHyNE) Resource (NSF ECCS- 1542205); the State of Illinois and International Institute for Nanotechnology (IIN). KI was partially supported by a Cluster Fellowship from the Institute for Sustainability and Energy at Northwestern (ISEN). SA acknowledges support from the "Designing Materials to Revolutionize and Engineer our Future" program of the National Science Foundation under Award No. 1729487

Notes and references

1 H. Tamaki, H. K. Sato and T. Kanno, *Advanced Materials*, 2016, **28**, 10182–10187.
2 J. Zhang, L. Song, S. H. Pedersen, H. Yin, L. T. Hung and B. B. Iversen, *Nature Communications*, 2017, **8**, 13901.

3 S. Ohno, K. Imasato, S. Anand, H. Tamaki, S. D. Kang, P. Gorai, H. K. Sato, E. S. Toberer, T. Kanno and G. J. Snyder, *Joule*, 2018, **2**, 1–14.
4 J. Mao, Y. Wu, S. Song, Q. Zhu, J. Shuai, Z. Liu, Y. Pei and Z. Ren, *ACS Energy Letters*, 2017, **2**, 2245–2250.
5 D. J. Singh and D. Parker, *Journal of Applied Physics*, 2013, **114**, 1–8.
6 W. Peng, G. Petretto, G.-m. Rignanese, G. Hautier, W. Peng, G. Petretto, G.-m. Rignanese and G. Hautier, *Joule*, 2018, 1–15.
7 K. Imasato, S. D. Kang, S. Ohno and G. J. Snyder, *Materials Horizons*, 2018, **5**, 59–64.
8 K. Imasato, S. D. Kang and G. J. Snyder, *Energy & Environmental Science*, 2019, **12**, 965–971.
9 Y. Wang, X. Zhang, Y. Wang, H. Liu and J. Zhang, *Physica Status Solidi (A) Applications and Materials Science*, 2019, **216**, 1–6.
10 J.-i. Tani and H. Ishikawa, *Materials Letters*, 2019, 127056.
11 K. Imasato, M. Wood, J. J. Kuo and G. J. Snyder, *Journal of Materials Chemistry A*, 2018, DOI: 10.1039/c8ta08975b.
12 J. i. Tani and H. Ishikawa, *Physica B: Condensed Matter*, 2020, **588**, 412173.
13 X. Shi, T. Zhao, X. Zhang, C. Sun, Z. Chen, S. Lin and W. Li, *Advanced Materials*, 2019, **31**, 1903387.
14 X. Shi, C. Sun, X. Zhang, Z. Chen, S. Lin, W. Li and Y. Pei, *Chemistry of Materials*, 2019, 3–10.
15 S. W. Song, J. Mao, M. Bordelon, R. He, Y. M. Wang, J. Shuai, J. Y. Sun, X. B. Lei, Z. S. F. Ren, S. Chen, S. Wilson, K. Nielsch, Q. Y. Zhang and Z. S. F. Ren, *Materials Today Physics journal*, 2019, **8**, 25–33.
16 J. J. Kuo, S. D. Kang, K. Imasato, H. Tamaki, S. Ohno, T. Kanno and G. J. Snyder, *Energy & Environmental Science*, 2018, **11**, 429–434.
17 Y. Wang, X. Zhang, Y.-Q. Liu, J.-X. Zhang and M. Yue, *Chinese Physics B*, 2020, **29**, 067201.
18 M. Wood, J. J. Kuo, K. Imasato and G. J. Snyder, *Advanced Materials*, 2019, **1902337**, 1–5.
19 M. Ozen, M. Yahyaoglu, C. Candolfi, I. Veremchuk, F. Kaiser, U. Burkhardt, G. J. Snyder, Y. Grin and U. Aydemir, *Journal of Materials Chemistry A*, 2021, **9**, 1733–1742.
20 Y. Lin, M. Wood, K. Imasato, J. J. Kuo, D. Lam, A. N. Mortazavi, T. J. Slade, S. A. Hodge, K. Xi, M. G. Kanatzidis, D. R. Clarke, M. C. Hersam and G. J. Snyder, *Energy & Environmental Science*, 2020, 4114–4121.
21 Y. Li, S. Zhang, F. Jia, S. Zheng, X. Shi, D. Jiang, S. Wang, G. Lu, L. Wu and Z.-G. Chen, *Materials Today Physics*, 2020, 135577.
22 J. I. Tani, M. Takahashi and H. Kido, *Physica B: Condensed Matter*, 2010, **405**, 4219–4225.
23 J. Mao, G. Chen and Z. Ren, *Nature Materials*, 2020, 41563–020.
24 Z. Liu, N. Sato, W. Gao, K. Yubuta, N. Kawamoto, M. Mitome, K. Kurashima, Y. Owada, K. Nagase, C.-H. Lee, J. Yi, K. Tsuchiya and T. Mori, *Joule*, 2021, **5**, 1–13.
25 Z. Liang, C. Xu, H. Shang, Q. Zhu, F. Ding, J. Mao and Z. Ren, *Materials Today Physics*, 2021, **19**, 100413.
26 J. Zhang and B. B. Iversen, *Journal of Applied Physics*, 2019, **126**, 085104.
27 M. Wood, K. Imasato and G. Je, *Journal of Materials Chemistry A*, 2020, available online.
28 H. Wang, S. Bai, L. Chen, A. Cuenat, G. Joshi, H. Kleinke, J. König, H. W. Lee, J. Martin, M. W. Oh, W. D. Porter, Z. Ren, J. Salvador, J. Sharp, P. Taylor, A. J. Thompson and Y. C. Tseng, *Journal of Electronic Materials*, 2015, **44**, 4482–4491.
29 J. Mao, H. Zhu, Z. Ding, Z. Liu, G. A. Gamage, G. Chen and Z. Ren, *Science*, 2019, **365**, 495–498.
30 Z. Han, Z. Gui, Y. B. Zhu, P. Qin, B.-P. Zhang, W. Zhang, L. Huang and W. Liu, *Research*, 2020, **2020**, 1672051.
31 X. Shi, C. Sun, Z. Bu, X. Zhang, Y. Wu, S. Lin and W. Li, *Advanced Science*, 2019, 1802286.
32 Y. Imai and A. Watanabe, *Journal of Materials Science*, 2006, **41**, 2435–2441.
33 A. A. Nayeb-Hashemi and J. B. Clark, *Bulletin of Alloy Phase Diagrams*, 1985, **6**, 432–434.
34 H. Okamoto, *Journal of Phase Equilibria and Diffusion*, 2010, **31**, 574.
35 A. A. Nayeb-Hashemi and J. B. Clark, *Bulletin of Alloy Phase Diagrams*, 1985, **6**, 528–533.
36 K. Imasato, S. D. Kang, S. Ohno and G. J. Snyder, *Materials Horizons*, 2017, **5**, 59–64.
37 J. Zhang, L. Song, K. A. Borup, M. R. V. Jørgensen and B. B. Iversen, *Advanced Energy Materials*, 2018, 1702776.
38 A. Zevalkink, D. M. Smiadak, J. L. Blackburn, A. J. Ferguson, M. L. Chabinyc, O. Delaire, J. Wang, K. Kovnir, J. Martin, L. T. Schelhas, T. D. Sparks, S. D. Kang, M. T. Dylla, G. J. Snyder, B. R. Ortiz and E. S. Toberer, *Applied Physics Reviews*, 2018, **5**, 021303.
39 S. Dongmin Kang, G. Jeffrey Snyder, S. D. Kang, G. J. Snyder, S. Dongmin Kang and G. Jeffrey Snyder, *Nature Materials*, 2016, **16**, 252–257.
40 G. J. Snyder, A. H. Snyder, M. Wood, R. Gurunathan, B. H. Snyder and C. Niu, *Advanced Materials*, 2020, 2001537.
41 A. F. May and G. J. Snyder, *Materials, Preparation, and Characterization in Thermoelectrics*, CRC Press, 2012, ch. 11, pp. 1–18.
42 H. S. Kim, Z. M. Gibbs, Y. Tang, H. Wang and G. J. Snyder, *APL Materials*, 2015, **3**, 1–6.
43 R. Gurunathan, R. Hanus and G. J. Snyder, *Materials Horizons*, 2020, **7**, 1452–1456.
44 W. Peng, G. Petretto, G. M. Rignanese, G. Hautier and A. Zevalkink, *Joule*, 2018, **2**, 1879–1893.
45 E. S. Toberer, A. Zevalkink and G. J. Snyder, *Journal of Materials Chemistry*, 2011, **21**, 15843–15852.
46 J. Yan, P. Gorai, B. Ortiz, S. Miller, S. A. Barnett, T. Mason, V. Stevanović and E. S. Toberer, *Energy and Environmental Science*, 2015, **8**, 983–994.
47 S. A. Miller, P. Gorai, B. R. Ortiz, A. Goyal, D. Gao, S. A. Barnett, T. O. Mason, G. J. Snyder, Q. Lv, V. Stevanović and E. S. Toberer, *Chemistry of Materials*, 2017, **29**, 2494–2501.
48 T. Kanno, H. Tamaki, H. K. Sato, S. D. Kang, S. Ohno, K. Imasato, J. J. Kuo, G. J. Snyder and Y. Miyazaki, *Applied Physics Letters*, 2018, **112**, 033903.
49 A. D. LaLonde, T. Ikeda and G. J. Snyder, *Review of Scientific Instruments*, 2011, **82**, 0.
50 K. A. Borup, J. de Boor, H. Wang, F. Drymiotis, F. Gascoin, X. Shi, L. D. Chen, M. I. Fedorov, E. Muller, B. B. Iversena and G. J. Snyder, *Energy & Environmental Science*, 2015, **8**, 423–435.
51 K. A. Borup, E. S. Toberer, L. D. Zoltan, G. Nakatsukasa, M. Errico, J.-P. P. Fleurial, B. B. Iversen and G. J. Snyder, *Review of Scientific Instruments*, 2012, **83**, 123902.
52 M. T. Agne, K. Imasato, S. Anand, K. Lee, S. K. Bux, A. Zevalkink, A. J. Rettie, D. Y. Chung, M. G. Kanatzidis and G. J. Snyder, *Materials Today Physics*, 2018, **6**, 83–88.
53 W. Kohn, A. D. Becke and R. G. Parr, *The Journal of Physical Chemistry*, 1996, **100**, 12974–12980.
54 G. Kresse and J. Furthmüller, *Physical Review B*, 1996, **54**, 11169.
55 J. P. Perdew, K. Burke and M. Ernzerhof, *Physical Review Letters*, 1996, **77**, 3865.
56 F. Tran and P. Blaha, *Physical review letters*, 2009, **102**, 226401.
57 J. W. Jaeken and S. Cottenier, *Computer Physics Communications*, 2016, **207**, 445–451.